PNAS RESEARCH ARTICLE | NEUROSCIENCE ENGINEERING

Doping-induced assembly interface for noninvasive in vivo local and systemic immunomodulation

Baoning Sha[a,b,c,d,e,f,g,h], Shengzhuo Zhao[a,b,c,d,e,i], Minling Gu[a,b,c,d,e,f], Dion Khodagholy[h], Liping Wang[a,b,c,d,e,f], Guo-Qiang Bi[a,b,c,d,e,j], and Zhanhong Du[a,b,c,d,e,f,1]

Edited by David Weitz, Harvard University, Cambridge, MA; received April 26, 2023; accepted October 23, 2023

Peripheral neural interfaces, potent in modulating local and systemic immune responses for disease treatment, face significant challenges due to the peripheral nerves' broad distribution in tissues like the fascia, periosteum, and skin. The incongruity between static electronic components and the dynamic, complex organization of the peripheral nervous system often leads to interface failure, stalling circuit research and clinical applications. To overcome these, we developed a self-assembling, tissue-adaptive electrode composed of a single-component cocktail nanosheet colloid, including dopants, conducting polymers, stabilizers, and an MXene catalyst. Delivered via a jet injector to designated nerve terminals, this assembly utilizes reactive oxygen species to catalytically dope poly (3,4-ethylenedioxythiophene), enhancing π–π interactions between nanosheets, and yielding a conductive, biodegradable interface. This interface effectively regulates local immune activity and promotes sensory and motor nerve functional restoration in nerve-injured mice, while engaging the vagal–adrenal axis in freely moving mice, eliciting catecholamine neurotransmitter release, and suppressing systemic cytokine storms. This innovative strategy specifically targets nerve substructures, bolstering local and systemic immune modulation, and paving the way for the development of self-adaptive dynamic neural interfaces.

neural interfaces | sensory and motor function | immune modulation | nanosheet composite | ROS-responsive self-assembly

Significance

In vivo neuroelectronics are crucial for addressing the burden of neural injury and neurological disorders. Enzymatic and electrochemical polymerization employed in neuroelectronics can conform to intricate anatomical structures but are constrained by diffusion stability, thus necessitating multicomponent syringe injections and covalent bonding. We present an MXene-catalytic doping system for assembling biodegradable neural interfaces. With reduced diffusivity, this system enables jet-injection application, creating reticular interfaces that align with the complex architecture of peripheral vagus nerve plexuses and exhibit distinct immune regulatory properties. We showcase local immune modulation for peripheral nerve repair and systemic regulation during immune storms. Our study unveils an innovative in vivo neuroelectronics fabrication method, laying the foundation for self-adaptive, biodegradable neural interfaces in multicircuit analysis.

The immune system is capable of instigating local and systemic diseases, such as diabetes (1), Crohn's disease (2), rheumatoid arthritis (3), and cytokine storm due to abnormally low or high activity levels. Electrical stimulation (ES) as a promising solution promotes nerve repair and immunomodulation through targeted stimulation and autonomic-central circuitry regulation (4). ES has been reported to promote neural repair through a series of calcium-dependent upregulations such as brain-derived neurotrophic factor (BDNF), nerve growth factor (NGF), and neurotrophin-3 (5). The design of neural interfaces varies significantly, with electrodes for local immune stimulation requiring excellent biocompatibility and specific substructures to support cell colonization and migration. Electrodes for peripheral neural circuits focus more on the stability and scalability of connections. Intrinsically elastic or morphing electronics have significantly enhanced biocompatibility and integration with both central and peripheral nervous systems (6, 7). This allows implanted devices like cuff electrodes or thin films to interact with extensive nerve branches, such as the sciatic nerve (8), and adapt to repetitive strains during movement (9). However, creating neural interfaces with numerous small nerves without eliciting immune response presents substantial microfabrication and microsurgery challenges for all cuff electrodes. Yet, establishing interfaces with autonomic nerves diffusely distributed in peripheral tissues like the fascia and periosteum during movement is a formidable task. This implies the necessity of creating neural interfaces with approximately 3,000 nerves of 50 to 300 μm each without triggering severe immune response, which poses substantial challenges for microfabrication and microsurgery (10). In response, efforts have been directed toward employing endogenous enzymatic activity to polymerize conducting polymer (CP) in vivo. Innovations in precursor design have successfully eradicated toxic reactions and ensured long-term stability and adaptability to various tissues. These advanced neural interfaces have significantly improved compatibility with complex neural substructures in both central and peripheral nervous systems. However, enzymatic polymerization depends on enzyme concentration and necessitates surfactants, increasing technical demands. This research adopts jet injection and self-assembly to tackle these issues.

We developed a versatile, monocomponent cocktail strategy for the in vivo assembly of biodegradable, self-adaptive neural interfaces that enable both local and global immunomodulation. To accomplish this regulation, we employed a propulsionary flow-enhancing method—jet-injection—to interface with a series of reticular nerve plexuses. Additionally,

The authors declare no competing interest.

This article is a PNAS Direct Submission.

[1]To whom correspondence may be addressed. Email: zh.du@siat.ac.cn.

This article contains supporting information online at https://www.pnas.org/lookup/suppl/doi:10.1073/pnas.2306777120/-/DCSupplemental.

Published November 30, 2023.

we engineered ROS (reactive oxygen species)-triggered catalytic doping nanosheets with inherently low diffusivity to counteract tissue diffusion during jet-injection. MXene, a semi-metal, has been widely studied for its conductivity, catalytic properties, and abundant surface functional groups (11). MXenes' catalase- and peroxidase-like performance have been proven to alleviate hypoxia and elevated oxidative stress in the tumor microenvironment (12). Another reason for choosing MXene is its unique interaction with cell membranes. The penetration of MXene nanosheets into cell membranes is a nonspontaneous process (13), demanding significantly more external force compared to other nanomaterials (14), which further enhances biosafety in jet-injection and helps reduce tissue dispersion. Therefore, we utilized MXene's catalase activity to catalyze the in vivo doping system, addressing the inherent challenge between catalyst functionality and conductivity (Fig. 1*A*). Furthermore, we functionalized MXene with de-doped CP–PEDOT [poly (3,4-ethylenedioxythiophene)] and the dopant–phenylsulfonic acid. The doping of de-doped PEDOT is mediated by the ROS-MXene cascade, which is triggered when the injection induces local microdamage, increases ROS metabolites in tissue, and subsequently prompts PEDOT doping by MXene. This doping process enhances the π–π interaction between nanosheets, promoting in vivo localization. In addition, we employed a tissue cross-linking compound, polydopamine (PDA), between de-doped PEDOT and benzenesulfonic acid dopant, which forms dynamic bonds with surround tissue during assembly, including hydrogen bonds, coordination bonds, cation–π interactions, and π–π interactions, further reducing diffusion. This composite system integrates all necessary reaction components including host matrix, dopant, and catalase in solid form, enhancing the system's resistance to tissue diffusion. In terms of potential long-term biotoxicity post-injection, extensive in vitro and in vivo characterizations were conducted, confirming the material's biocompatibility and biodegradation through the oxidative breakdown of MXene (15). The injected neural interface, established with the sciatic nerve, can promote peripheral tissue recovery through local regulation via electrical stimulation. In freely moving mice, the neural interface activated the vagal anti-inflammatory axis at the hindlimb Zusanli (ST36) acupoint, releasing noradrenaline, adrenaline, and dopamine from adrenal

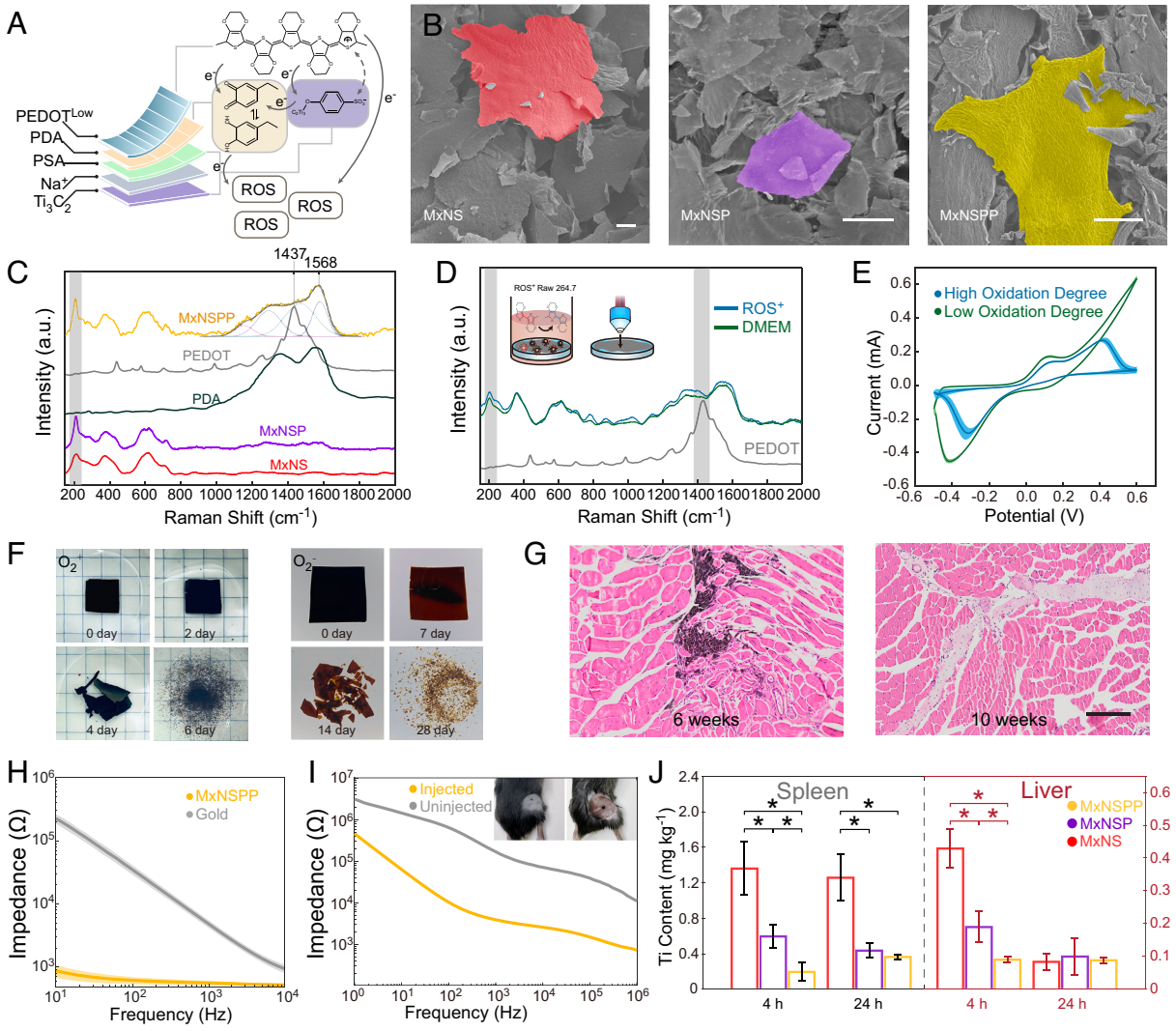

Fig. 1. In vitro and in vivo characterization of jet-injected neural interface. (*A*) Illustrations of MxNSPP nanosheet composite and ROS responsive properties. (*B*) SEM images of sulfonic MXene nanosheets (MxNS), PDA functionalized sulfonic MXene nanosheets (MxNSP), and MxNSPP (Scale bar: 20 μm.) (*C*) Raman spectra of PDA, PEDOT, MxNS, MxNSP, and MxNSPP. (*D*) Raman spectra of MxNSPP cultured with ROS+ Raw 264.7 cell and culture media. (*E*) Redox activities of MxNSPP with degrees oxidation degrees. (*F*) Biodegradation of MxNSPP in PBS (pH 7.4) at 85 °C in air and in nitrogen. (*G*) In vivo degradation of MxNSPP in mouse peripheral tissue (Scale bar: 200 μm). (*H*) Electrochemical impedance spectroscopy (EIS) measurements of gold electrode and MXene-NSD-PEDOT decorated electrode. (*I*) EIS measurements of MxNSPP jet-injected interface and none-injected interface. (*J*) Aggregation of nanosheets in the spleen and liver after injection (n = 3). * indicates a statistical difference from MxNSPP groups ($P < 0.05$). All statistical analyses were performed by one-way ANOVA.

chromaffin cells while reducing TNF (tumor necrosis factor) and IL-6 (interleukin 6) levels in serum. We demonstrate that catalytic doping and cross-linking around peripheral tissue create biodegradable, self-adaptive interfaces with reticular nerve plexuses in peripheral–central circuitry.

Results

Synthesis and Characterization of MxNSPP Nanosheets. We synthesized ROS-responsive PDA-PEDOT functionalized sulfonic MXene nanosheets (MxNSPP) by surface modification and self-assembly in solution (Fig. 1*A*). Additionally, we synthesized nanosheets without the PEDOT layer (MxNSP) and nanosheets without the PEDOT and PDA layer (MxNS) to study the effect of different layers on self-assembly and immune response. Differences in morphology and thickness among MxNSPP, MxNSP, and MxNS were observed through scanning electron microscopy (SEM) and atomic force microscopy (AFM) (Fig. 1*B* and *SI Appendix*, Fig. S1*A*). The FTIR (Fourier transform infrared) spectrum and energy-dispersive spectroscopy of MxNSPP nanosheets revealed the presence of phenylsulfonic acid group, PDA, and PEDOT (*SI Appendix*, Fig. S1 *B* and *C*). X-ray diffraction (XRD) of MxNS showed a large shoulder on the (002) peak and a weakening of the (004) and (006) peaks, indicating a disruption of periodicity in aromatic compounds. This suggests that stacked pieces of Ti_3C_2 sheets are rather rare (*SI Appendix*, Fig. S1*D*) (16). The Raman spectra showed a band at 1,568 cm^{-1} corresponding to PDA's C=O catechol stretching vibrations (Fig. 1*C*) (16, 17), while the peak at 1,437 cm^{-1} corresponded to C=C symmetric vibrations, indicating that the PEDOT layer in MxNSPP was less oxidized and more of a benzoin structure than $Fe3^+$-catalyzed PEDOT. The intensity of the A_{1g} (Ti, O, C) peak at 214 cm^{-1} indicated a more uniform orientation and reduced defect density in MxNSPP (18, 19). Finally, we observed the absence of D and G bands after phenylsulfonic acid diazonium intercalation, which might suggest the deformation of carbon (20, 21).

In Vitro and In Vivo Validation of ROS-Responsive Self-Assembly with Jet-Injection. We hypothesized that the catalytic electron transfer that promotes EDOT polymerization in vivo could also facilitate PEDOT reconfiguration (22–24). We observed alterations in MxNSPP in Raman spectroscopy when co-cultured with ROS+ macrophages (Fig. 1*D*). The peak at 214 cm^{-1} shows enhanced nanosheet contact and higher nanosheet stacking (18, 25) after cocultured with ROS^+ macrophage. The red-shift of the Cα=Cβ band of the ROS^+ group at around 1,430 cm^{-1} suggested that the PEDOT layer transitioned from benzoin to quinoid. The quinoid structure has a more linear or expanded-coil structure and more robust π–π contacts between chains, increasing Van der Waals forces. We evaluated the redox behavior of MxNSPP at various oxidation degrees using cyclic voltammetry (CV) (Fig. 1*E*). The oxidative peaks at 0.13 V and −0.41 V corresponded to the catechol-quinone transformation in the PDA layer (26). After further oxidation of MxNSPP, a peak at 0.41 V developed, corresponding to Ti_3C_2 lattice oxidation. The two redox peaks had similar intensities, indicating that highly oxidized MxNSPP still contained enough catechol groups. We observed different oxidative breakdown speeds with and without O_2 in PBS solution to mimic the biological environment (Fig. 1*F*). The MxNSPP colloid displayed adequate rheological characteristics for jet-injection and had an average size of 132 nm (*SI Appendix*, Fig. S1 *E* and *F*) (27–29). In an in vivo jet-injection study, we tracked the biodegradation of MxNSPP nanosheets injected into muscle tissue. Ten weeks post-injection, localized nanosheets could no longer be observed in the fascia and surrounding tissues (Fig. 1*G*). We also characterized the MxNSPP's potential in reducing gold electrode impedance and the MxNSPP jet-injection impedance (Fig. 1 *H* and *I*). The results showed MxNSPP coated on gold increased the electrode's Ohmic contact and jet-injected MxNSPP reduced cross-tissue impedance, which is similar to patch electrodes (PEs) (30) and in vivo polymerization electrodes (31). Furthermore, a resistance decrease is noted at the stimulation frequency of 20 Hz.

To ensure high injectant localization and low organ accumulation, we tested the biodistribution and in vivo self-assembly of MxNSPP. Nanosheets were jet-injected into mice's sciatic nerves through the gap between the gluteal and hamstring muscles. The low Ti contents in MXene enrichment organs 4 and 24 h after injection suggested that MxNSPP localized before complete oxidation (Fig. 1*J*). Five days after injection, the injected tissue was collected and stained with hematoxylin and eosin (H&E) (Fig. 2*A*). MxNSPP jet-injectant exhibited enhanced aggregation, tissue attachment, and reduced lymphocyte infiltration. The biosafety test showed no evidence of nanosheet organ damage (*SI Appendix*, Fig. S2*A*).

In Vitro Cellular Behavior and Immune Modulation. We investigated the biocompatibility of MxNSPP and its potential to modulate local cellular immune responses (32–34). MxNSPP exhibited a lower zeta potential, increased hydrophobicity, which are known to promote cell adhesion and migration (*SI Appendix*, Fig. S2 *B* and *C*). To study cell proliferation and differentiation on nanosheets with and without ES, we used rat pheochromocytoma (PC12) cells. The PC12 cells were seeded and cultured for 1 d before being stimulated for 1.5 h with varying constant voltages (30 mV, 60 mV, and 120 mV) in a customized stimulator (*SI Appendix*, Fig. S3*A*). Most cells cultured on MxNSPP displayed short axons, indicating that MxNSPP nanosheets may encourage PC12 cell spreading (*SI Appendix*, Fig. S3*B*). The ES-treated groups outperformed the ES-free groups in spreading performance, and as the voltage increased, the ES-treated groups showed increased cell number, axonal number, and axonal length (*SI Appendix*, Fig. S3 *C–E*), which shows similar potential to promote cell differentiation as previous research (35).

Schwann cells (SCs) play a crucial role in nerve repair. In the initial 3 d following damage, macrophages and SCs clear up the axons and myelin detritus (36). SCs then proliferate and transdifferentiate into specialized repair cells that fill the empty endoneurium tubes and form Büngner bands (37, 38). Additionally, SCs release neurotrophic factors such as BDNF, glial cell-derived neurotrophic factor (GDNF), NGF, and vascular endothelial growth factor (VEGF), which promote axon growth toward damaged neurons (39, 40). To investigate cell migration, we cultured SCs on MxNSPP or MxNS patterned coverslips (Fig. 2*B* and *SI Appendix*, Fig. S4*A*). The SCs on MxNSPP predominantly attached to the MxNSPP pattern with long pseudopods interacting with neighboring cells, exhibiting a longer average length and improved viability/cytotoxicity (Fig. 2 *C–E*). We co-cultured SCs with MxNSPP in the upper chambers of transwells, cultured PC12 in the bottom chamber, and observed PC12 differentiation (*SI Appendix*, Fig. S4 *B* and *C*). We then examined the expression of neurotrophic factors in SCs cultured on MxNSPP with qPCR and detected an increase in the expressions of BDNF, GDNF, NGF, and VEGF (*SI Appendix*, Fig. S4*D*), which indicates that MxNSPP can up-regulate the expression of BDNF, GDNF, and NGF in SCs and, through these factors, influence PC12 differentiation.

Maintaining low levels of oxidative stress by ROS is crucial for neural repair through immune regulation (41, 42). We initially tested distinct oxidative degradation processes induced by hydrogen peroxide, on different self-supporting films of nanomaterials. Notably, the MxNSPP membrane exhibited enhanced stability and an extended

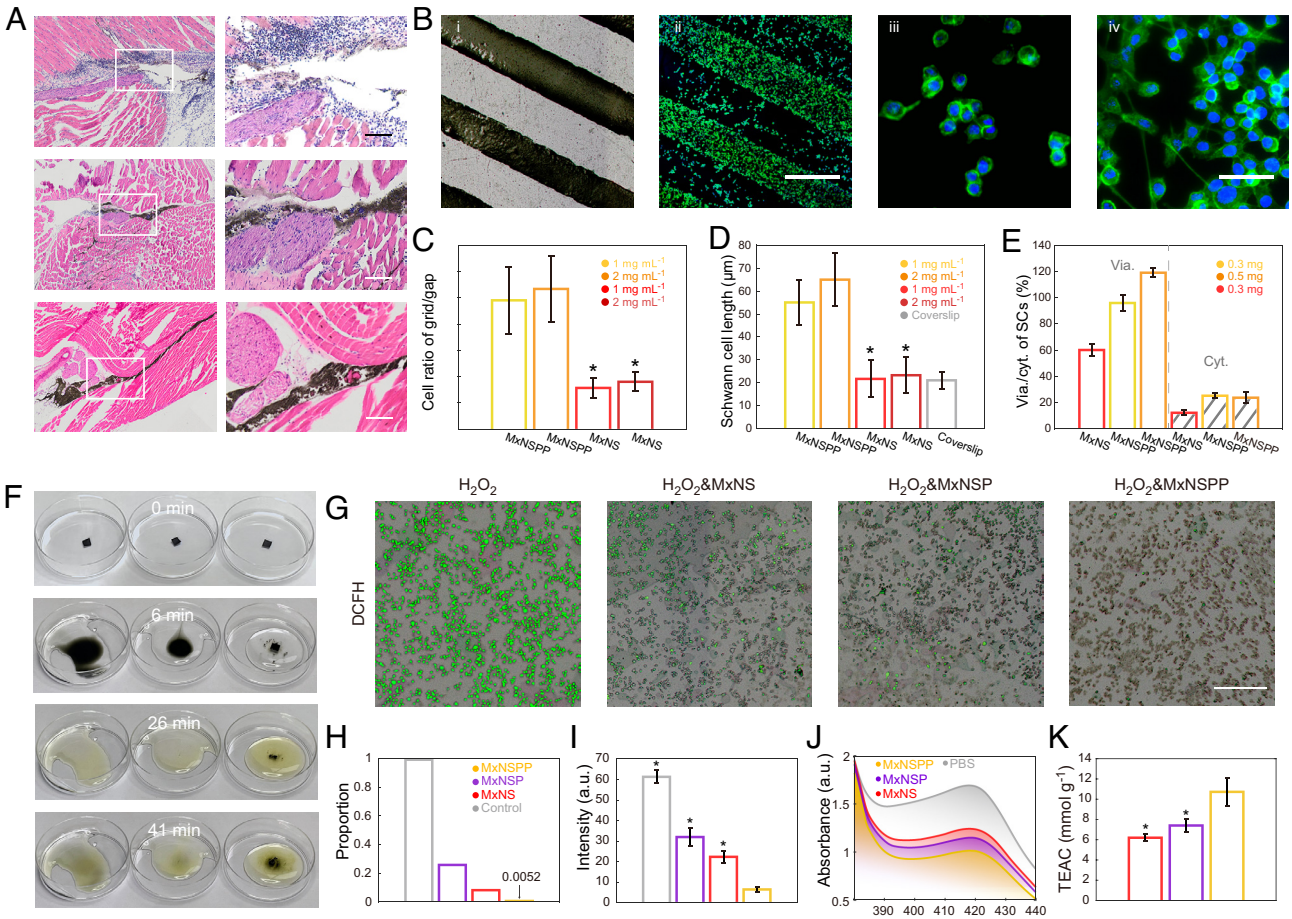

Fig. 2. MxNSPP regulated the cellular activity of local nerve damage. (*A*) Diffusion of jet-injected nanosheets in sciatic nerve surrounding tissues with H&E staining (Scale bar: 200 μm.) (*B*) Bright-field; i) and fluorescence; ii) images of SCs cultured on MxNSPP pattern (Scale bar: 500 μm); fluorescence images of SCs at the gap; iii) and the grid pattern; iv) (Scale bar: 50 μm.) (*C*) Ratio of the cells on the grid to the cells on the gap (n = 3). (*D*) Average lengths of SCs cultured on MxNSPP, MxNS, and coverslips (n = 10). (*E*) Viability and cytotoxicity of SCs measured with Calcein/PI assay (n = 3). (*F*) Resistance and catalytic decomposition of nanosheet-filtered membrane (*Left* to *Right*: MxNS, MxNSP, and MxNSPP) in H_2O_2. (*G*) Intracellular ROS-scavenging performance of MxNS, MxNSP, and MxNSPP (Scale bar: 400 μm.) (*H*) Proportion of cells with significant fluorescence after different nanosheet treatments. (*I*) Fluorescence intensity of cells after different nanosheet treatments (n = 3). (*J*) UV–vis spectra of ABTS after reaction with PBS, MxNS, MxNSP, and MxNSPP. (*K*) Trolox-equivalent antioxidant capacity (TEAC) of the nanosheets (n = 3). * indicates a statistical difference from MxNSPP groups ($P < 0.05$). All statistical analyses were performed by one-way ANOVA.

degradation lifespan (Fig. 2*F* and Movie S1). We characterized the potential of MxNSPP eliminating ROS in vitro by quantifying macrophage oxidative stress with dichlorofluorescein (DCFH). In the macrophage-nanosheet coculture experiment, ROS^+ macrophages grown in a media containing MxNSPP exhibited the lowest ROS level (Fig. 2 *G–I*). Further, we used the Trolox-equivalent antioxidant capacity (TEAC) test to quantify nanosheets' antioxidant capacity. MxNSPP, exhibited a TEAC of 10.7 mmol g^{-1}, higher than MxNS's 6.2 mmol g^{-1} and MxNSP's 7.4 mmol g^{-1}, indicating increased ROS-scavenging capability than MxNS and MxNSP (Fig. 2 *J* and *K*). In SCs and macrophage co-culture, we observed an enhanced SC migration through the transwell film (*SI Appendix*, Fig. S5 *A* and *B*). Furthermore, macrophages grown on MxNSPP elevated the expression of arginase 1 (arg1) and interleukin 10 (IL10), indicative of M2 polarization, which corresponds to the shift from a pro-inflammatory to an anti-inflammatory phenotype in macrophages (*SI Appendix*, Fig. S5 *C* and *D*). These findings suggest that MxNSPP could effectively modulate the immune response and promote neural repair by scavenging ROS and promoting M2 polarization.

Jet-Injected MxNSPP Interface Can Modulate Local Inflammatory Responses and Facilitate Nerve Repair. Abnormal local immune response is a significant obstacle to nerve recovery in various nerve injuries. ES has been found to boost early phases of regeneration, including neuronal survival and axonal sprouting (43). We investigated whether the MxNSPP interface could impact local inflammatory response and guide neurorehabilitation using a sciatic nerve crush (SNC) model (Fig. 3*A*). Two days after SNC, MxNSPP colloid was injected into the injured nerve through the gap between the gluteal and hamstring muscles using a jet-injection method. Three days later, the injected tissue was collected and stained for CCR7 (red) and CD206 (green) to analyze the M2/M1 phenotype of recruited and activated macrophages (Fig. 3 *B* and *C*). Most macrophages were found in the surrounding tissue of the nerve, and the M2/M1 ratio in the MxNSPP group was greater than in the MxNS and MxNSP groups, suggesting increased M2 polarization.

We used the PE to connect the MxNSPP jet-injectant at the injection site for ES. Twelve hours after jet-injection, we applied PE to the injection site to perform low-intensity ES (3V). To investigate the survival and recruitment of SCs, we stained for S100 (Fig. 3 *D* and *E*). The density of SCs decreased as they approached the site of damage in all groups (Fig. 4*D*). However, the jet-injected ES group retained 50% of the SC density at 800 m past the crushed location, which was greater than the injected and control groups. The distribution of SCs in the jet-injected ES group may be attributed to either a reduction in the rate of SCs apoptosis induced by ES or to the subsequent migration of these cells. Histological staining of

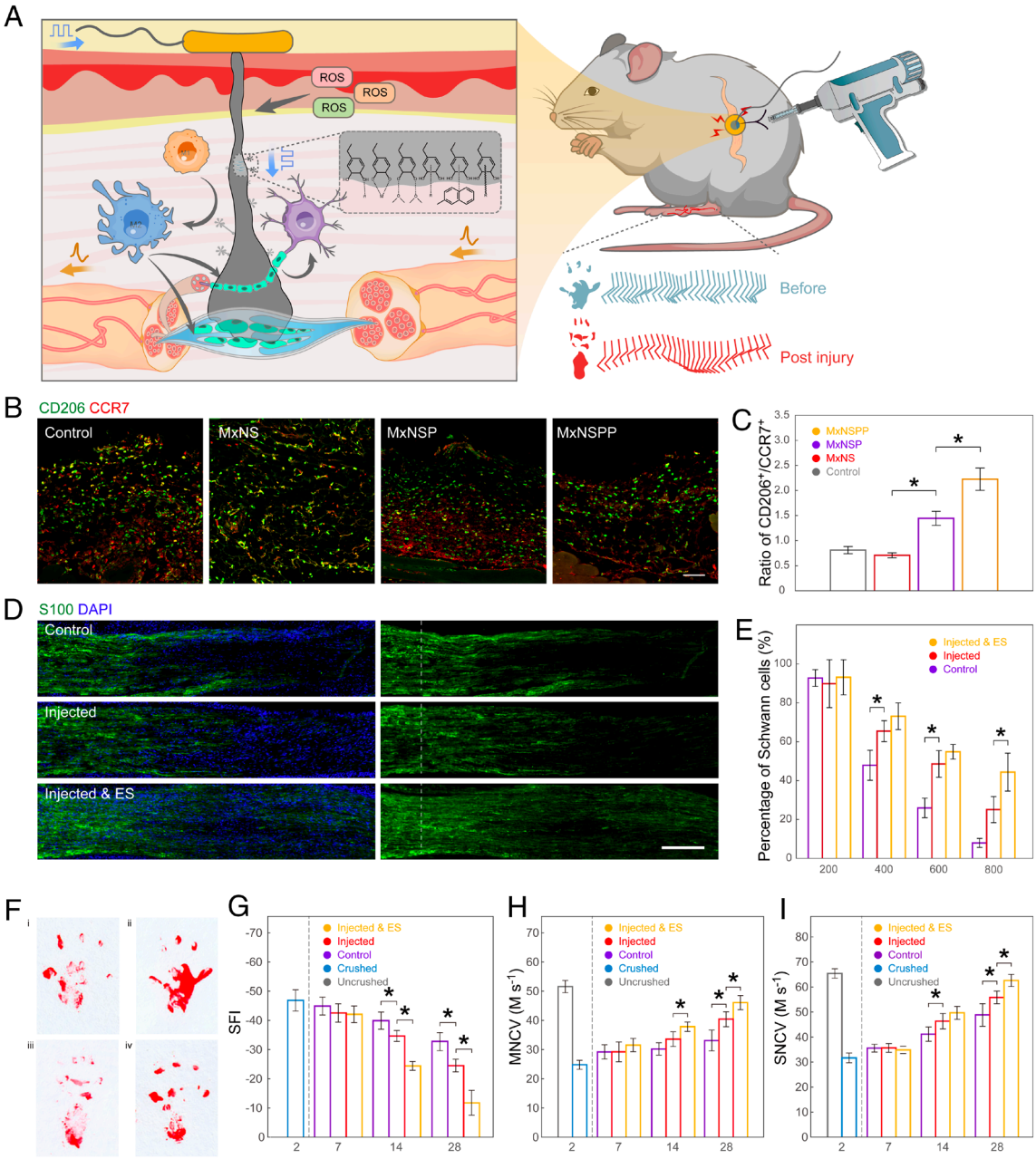

Fig. 3. Jet-injected neural interface promoted the recovery of motor and sensory nerves in peripheral nerve injury. (*A*) Injected neural interface regulated immune responses between macrophages, SCs, and neurons, facilitating cellular migration and nerve recovery. (*B*) Immunofluorescent images of CD206+ (green) CCR7+ (red) macrophages in SNC models injected with different nanosheets or saline as control (Scale bar: 200 μm.) (*C*) Quantitative analysis of CD206+/CCR7+ macrophages in different groups (n = 3). (*D*) Immunofluorescent images of S100+ SCs in SNC representative sections (Scale bar: 200 μm.) (*E*) Quantitative analysis of the percentage of SCs past the crush site normalized to the fluorescence intensity at the crush site plotted as a function of the distance from the crush site (n = 3). (*F*) Footprint stamps in walking track analysis (i interface injected with ES, ii uncrushed, iii control, and iv interface injected without ES). (*G*) Quantitative analysis of SFI (n = 5). (*G*) Motor nerve conduction velocity of SNC mice (n = 5). (*H*) Motor nerve conduction velocity of SNC mice (n = 5). (*I*) Sensory nerve conduction velocity. The mice SNC was made on day 0. ES was applied every 2 d since day 2 (n = 5). * indicates a statistical difference ($P < 0.05$). All statistical analyses were performed by one-way ANOVA.

slices before ES revealed significant disintegration of SCs, suggesting that the observed recovery of these cells is likely migration-driven (*SI Appendix*, Fig. S6*A*). The secretion of signaling molecules by SC is crucial for altering the local immune response environment, which in turn affects local nerve regeneration, this aligns with the results of our nerve fiber staining using Neurofilament 200 antibody (NF200)(*SI Appendix*, Fig. S6 *B* and *C*) The ES modulation effect with our device can have a substantial impact on the recruitment of SC, indirectly influencing the local immune response to promote more rapid and effective nerve regeneration. The ES-induced functional recovery of the sciatic nerve was further demonstrated by the restoration of the sciatic nerve function index (SFI), motor nerve conduction velocity, and sensory nerve conduction velocity (SNCV) (Fig. 3 *F*–*I*). We also investigated how ES improved sensory recovery following SNC. Anti-PGP9.5 immunostaining of the paw interdigital skin 16 d after injury revealed a considerable increase in epidermal innervation in the injected ES group, coinciding with SNCV healing (*SI Appendix*, Fig. S6 *D*–*F*). The restoration of sensitivity to mechanical allodynia was observed after day 10 (*SI Appendix*, Fig. S6*G*). These findings suggest that ES with the

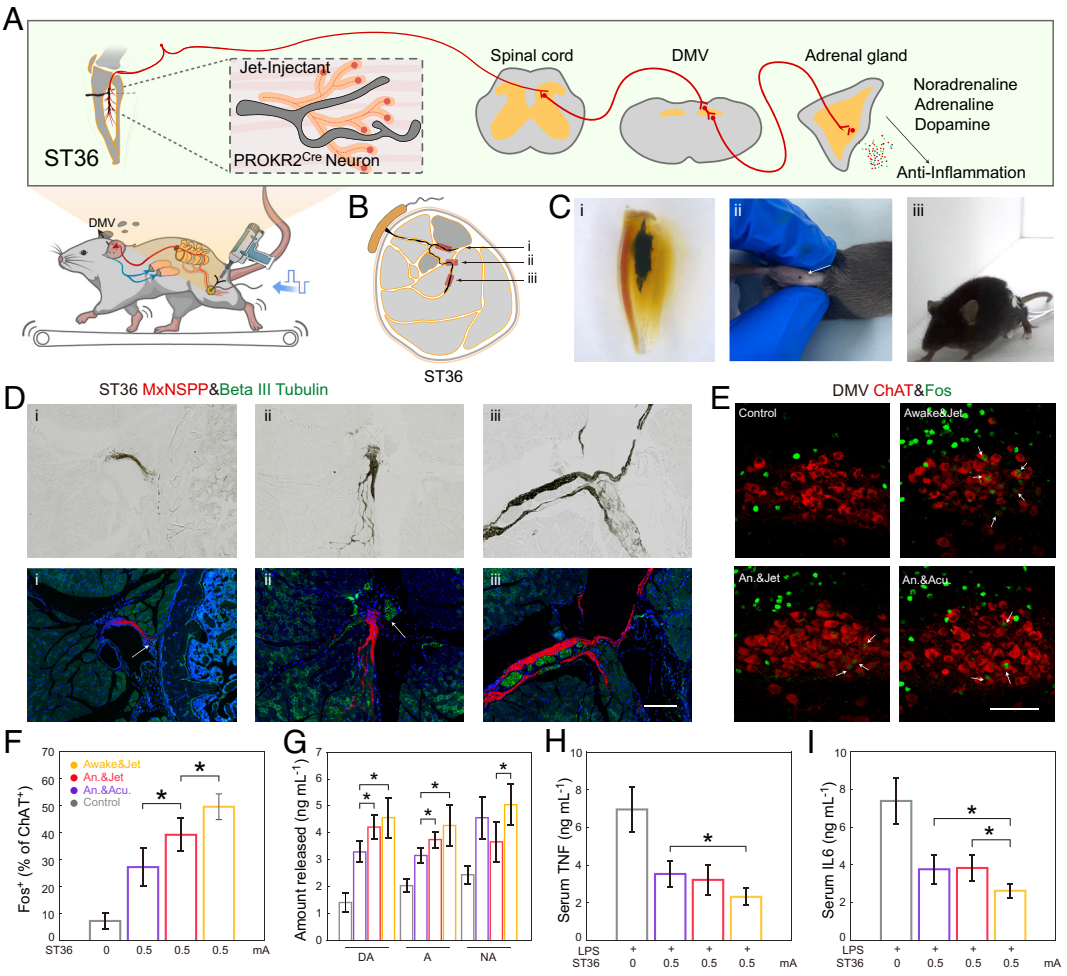

Fig. 4. Jet-injected nerve interface drove the vagal–adrenal anti-inflammatory axis with low-intensity ES in awake mice. (*A*) Electrode stimulation at the ST36 site activates PROKR2Cre neurons, leading to DMV engagement and subsequent release of anti-inflammatory mediators via the vagal–adrenal axis. (*B*) Vagal–adrenal axis driven by PROKR2Cre neurons innervating deep limb fascia and periosteum. (*C*) The lower leg with Jet-injected nerve interface after clearing (i); the injection point of the jet-injected interface (ii); mice under ES (iii). (*D*) Brightfield and immunofluorescent images of jet-injected nerve interface and Beta III Tubulin+ nerves, corresponding to the i, ii, and iii in Fig. 4*B* (Scale bar: 200 μm.) (*E*) Immunofluorescent images of c-Fos expression (green) induced by ES (0.5 mA) at the ST36 acupoint in ChAT+ (red) DMV neurons (Scale bar: 100 μm.) (*F*) Quantitative analysis of the percentage of c-Fos expression (green) in ChAT+ (red) DMV neurons (n = 5). (*G*) ST36 site ES increased noradrenaline (NA), adrenaline (A), and dopamine (DA) release (n = 5). (*H* and *I*) ST36 site ES decreased TNF and IL-6 level in LPS-induced infection (n = 5). * indicates a statistical difference ($P < 0.05$) form Awake&Jet group. All statistical analyses were performed by one-way ANOVA.

jet-injected interface can promote motor and sensory recovery by increasing macrophage polarization, SC migration, and epidermal innervation.

Jet-Injected MxNSPP Interface Can Inhibit Systemic Cytokine Release Syndrome. In investigations of neuromodulatory therapies for illnesses mediated by systemic immune responses, global immune responses often lead to changes in animal behavior and pain response, making the findings difficult to interpret. Moreover, implantation of neural interfaces can change the normal physiological environment, causing foreign body reactions and neuropathic pain. To assess whether the jet-injected interface induces neuropathic pain, we examined the parabrachial nucleus circuit activity and behavioral changes in mice following implantation. Our results showed no significant difference between the experimental and control groups in the activation of pain-promoting glutamatergic neurons in the lateral parabrachial nucleus, and the mice showed no differences in responses to von Frey and hot plate tests (*SI Appendix*, Fig. S7 *A–D*). These findings suggest that the implantation process did not cause acute discomfort. In addition, the implanted electrodes' movement can lead to friction and shear damage to nearby nerve and muscle tissue, causing discomfort and behavioral abnormalities. To evaluate the impact of the jet-injected interface on behavior and movement, we compared the movement characteristics of mice exercising on a treadmill with and without the injection. Stride frequency and joint angle remained constant, and movements could be classified into two groups using principal component analysis, demonstrating that the neural interface does not cause discomfort during or after implantation and can maintain behavioral performance during movement (*SI Appendix*, Fig. S7 *E–H*).

The vagus anti-inflammatory circuit's anatomy was recently documented. For the treatment of severe cytokine release disorders, electroacupuncture at the ST36 (Zusanli) acupuncture point can regulate the vagal–adrenal axis (44). However, the PROKR2^{Cre} neuron that broadly innervates deep fascia and periosteum during development rarely distributes in superficial tissues such as skin, making the interface challenging. Additionally, in awake animals, severe foreign body sensation and muscle twitching during stimulation can interfere with electroacupuncture, resulting in most studies being conducted in anesthetized animals. However, anesthetics like isopentane and pentobarbital sodium may alter the firing intensity of animal neurons, potentially influencing the accuracy of the results.

We explored the jet-injected interface's capability to stimulate the vagal–adrenal axis in conscious animals. This was achieved by administering electrical stimulation (ES) at the ST36 acupoint on the hindlimb, transmitting through the spinal cord and the dorsal motor nuclei of the vagus (DMV) to the adrenal gland (Fig. 4*A*). Bilateral placement of the MxNSPP interface or acupuncture needles was made into the tibialis anterior muscles near the peroneal nerves (Fig. 4*B*), while PEs were connected to the injection site and the homolateral skin above the biceps femoris (BF) muscle (Fig. 4*C* and Movie S2). Immunofluorescence results revealed that the jet-injected interface (red) connected with neurons in the fascia and periosteum (green) (Fig. 4*D*). Low-intensity (0.5 mA) ES produced Fos expression (green) in choline acetyltransferase (ChAT)-identified hindbrain vagal efferent neurons of the DMV (Fig. 4*E*). In awake mice, the jet-injected interface elicited a 50% maximum activation, while the anesthetized jet-injected group's 40% was more significant than the electroacupuncture group's 30% and the prior study's 33% (Fig. 4*F*). Using an ELISA, we also demonstrated that ES at ST36 induced the release of noradrenaline (NA), adrenaline (A), and dopamine(DA) from adrenal chromaffin cells (Fig. 4*G*), which indicates that the vagal–adrenal axis was activated by low-intensity ES and can promote the secretion of anti-inflammatory transmitters (44).

We examined the ability of the jet-injected interface to activate the vagal–adrenal axis, inhibiting the systemic cytokine release induced by lipopolysaccharide (LPS). When electrical stimulation (ES) was administered at ST36, there was a marked reduction, over 50%, in inflammatory markers—TNF and IL-6—in LPS-treated control littermates, a significant finding observed in the awake jet-injected group (Fig. 4 *H* and *I*). Fos labeled neurons in the rostral ventral lateral medulla (rVLM) did not show significant changes between groups, indicating that the jet-injected interface did not trigger sympathetic reflexes (*SI Appendix*, Fig. S7 *I* and *J*). These results suggest that ES with a jet-injected interface can induce anti-inflammatory responses via the vagal–adrenal axis instead of spinal sympathetic responses. Additionally, stronger connections and awake stimulation enhanced the activity of hindbrain vagal efferent neurons.

Discussion

In this study, we propose a local and systematic immunomodulation method that involves the structural alteration of electroactive polymers and dynamic redox adhesiveness of PDA on specific nerves. Compared to previous methods based on pre-polymer and monomer, this ROS-responsive self-assembly provides better control over biotoxicity and biodegradation during injection and stimulation. By extending the electron transfer strategy between nanosheets and forming complex multiple electron donors and receptors, it may be possible to achieve highly time-precise regulation of post-injection redox adhesion, polymer reconfiguration, and oxidative degradation. The further development of electroactive polymers could improve the efficiency of in vivo self-assembly. We anticipate that high tissue adhesion and controlled degradation of the assembled implant can be achieved through exogenous or endogenous oxidation of the basal MXene structure.

Furthermore, expanding the nanomaterial assembly strategy to gene-targeted polymerization, which involves synchronously targeting cells to synthesize conducting or nonconducting polymers at the tip of the injectant, can enable the stimulation and recording of specific cells or nerves. The development of genetically targeted photosensitizers can also permit the control of the polymer assembly process in time and space to form desired subcellular structures and reduce the in vivo diffusion of materials. We anticipate that the advancement of in vivo assembly materials will further enable the regulation of the peripheral–central axis, leading to the in vivo control of animal behavior, cognition, and immunity. Finally, the monomer-free in vivo self-assembly of nanomaterials demonstrates the practicality of a multistrategy coordinated electrode assembly for neural interfaces. This approach offers a more comprehensive connection to targeting nerves, which has the potential to provide greater feedback and regulation capabilities at the system level compared to conventional strategies.

Materials and Methods

Materials. Hydrofluoric acid, ethanol absolute, and sodium hydroxide were purchased from Shanghai Lingfeng Chemical Reagent. Sodium nitrite and dopamine hydrochloride were purchased from Macklin. Argon gas was purchased from Hongzhou Industrial Gas Company. Ti_3AlC_2 ceramic was purchased from Laizhou Kaiene Ceramics. Deionized water was purified using the Milli-Q Direct 8 instrument. All other chemicals were purchased from Aladdin and were used without further purification. Adult (20 g to 30 g) male C57BL/6 mice (Guangdong Medical Laboratory Animal Center) aged 6 to 8 wk were used for the experiments. All animal experiments were approved by the Institutional Animal Care and Use Committee of Shenzhen Institutes of Advanced Technology, Chinese Academy of Sciences.

Synthesis of MxNSPP Nanosheets. First, 3 g Ti_3AlC_2 ceramic powder was slowly immersed into a polytetrafluoroethylene beaker containing 40 mL HF aqueous solution and stirred at room temperature for 48 h. The resulting suspension was then transferred to a centrifuge tube and centrifuged at 20,000 rpm for 5 min. The wet precipitate was washed with deionized water and centrifuged several times. After decanting the liquid in the last step, 30 mL (5 wt%) NaOH solution was added dropwise into the centrifuge tube. The solution was transferred to a beaker and stirred for 2 h. The product was centrifuged and washed several times with a large amount of deionized water until the pH of the top liquid was 7 to 8. Then, the obtained nanosheets were redispersed in 10 mL of deionized water. Phenylsulfonic acid diazonium salt was obtained using the literature protocol: 6.3 g sulfanilic acid was suspended in 30 mL water and cooled to 0 to 5 °C. A solution of 9 mL HCl and 30 mL water was pre-cooled to 0 to 5 °C and slowly added to the suspension with stirring under ice bath conditions. After 15 min, a cold solution of 2.4 g sodium nitrite (18 mL) was added dropwise to the rest and stirred for 30 min to obtain a diazonium salt solution. The diazonium salt solution synthesized above was added dropwise to the nanosheet dispersion in an ice bath with stirring, and the mixture was kept at 0 to 5 °C for about 4 h. After the reaction, the mixture was washed several times and then centrifuged at 4,000 rpm for 1 h to separate large aggregates and unreacted particles. Then, the supernatant was lyophilized into MxNS powder. The obtained powder was dispersed with 60 mL deionized water at a concentration of 2.5 mg mL^{-1}, and 15 mL Tris-HCl solution (pH 8.5) was added dropwise to the solution. At the same time, 15 mg DA was added to 15 mL Tris-HCl solution (pH 8.5) and stirred for 15 min for pre-polymerization. Then the DA pre-polymerized solution was added dropwise to the MxNS solution and stirred for 4 h to obtain the MxNSP nanosheets. The MxNSP nanosheets were centrifuged, washed several times, and redispersed with 60 mL deionized water. Finally, 160 μL EDOT was dissolved in 10 mL ethanol; then, the EDOT solution was added dropwise to the MxNSP solution and stirred at room temperature for 24 h. Afterward, the solution was centrifuged, washed several times, and lyophilized to obtain MxNSPP nanosheets.

Nanosheet Characterization. The morphologies of the nanosheets were observed using SEM. The samples were lyophilized and then put on an SEM sample platform (Ted Pella) to be sputter-coated with a thin layer of gold. The nanosheets were imaged at ×300 magnification and operated at 5 kV (MERLIN, ZEISS, Germany). The thickness was measured using AFM. The samples were dispersed in water (5 μg mL^{-1}) and ultrasonically dispersed (200 W) for 30 min. The dispersion was then dropped on a quartz plate and vacuum dried. The nanosheets were imaged at 9 μm^2 using an AFM (Dimension Ico, Bruker, Germany). The XRD was measured with an XRD system (SmartLab, Rigaku, Japan). The samples were lyophilized and then Pressed into a mold platform (25 mm^2) and measured using a Cu radiation source (1.54056 Å) at 40 kV. The FTIR spectrum was measured with an infrared spectrometer (VERTEX70, Bruker, Germany). The lyophilized samples were mixed with iodine bromide powder, pressed in a mode (15 to 16 MPa, 1 min), and then

analyzed. The energy-dispersive X-ray spectrum of the MxNSPP nanosheets was measured using SEM. (MERLIN, ZEISS, Germany). The Raman spectra were measured with a micro-Raman spectrometer (LabRam HR Visible, Horiba Jobin Yvon, France). The samples were lyophilized, put on an object slide, and measured with a 633 nm laser at 1 mW. The water contact angle was measured on the self-supporting membrane with a horizontal microscope (SHL Tech, Shenzhen, China). The freeze-dried MxNSPP nanosheets were dispersed in 20 mL deionized water (3 mg mL^{-1}). The dispersion was filtered into a self-supporting membrane by vacuum suction filtration. The water contact angle was measured 10 s after adding 0.4 μL deionized water on the membrane surface. The size distributions and zeta potentials were measured with a particle size analyzer (MS2000, Malvern, UK) at 25 °C. The rheological properties were measured using a rheometer (MCR302, Anton parr, Austria) after dispersing the nanosheets in deionized water (5 mg mL^{-1}) at 25 °C.

Performance of Jet-Injected Interface. Male C57BL/6J mice were anesthetized with isoflurane (5% induction, 2% maintenance), shaved on the hind limbs and lower back, and sterilized with iodine. The mice were laced on a heating pad to maintain body temperature. An ophthalmic solution was applied to the eyes to prevent drying. Then, 40 μL 5 mg mL^{-1} MxNSPP dispersion was injected into the sciatic nerve in the right thigh between the gluteal and hamstring muscles. Five hours later, The mice were killed and an acupuncture needle was applied at the injected sight as the working electrode. An acupuncture electrode (R = 2 mm) was inserted in the ipsilateral calf. During the measurement, the calf of the mouse was naturally extended with the knee at 90°. The impedance was measured on an electrochemical system (GAMRY Reference 600, USA). The AC voltage was 10 mV RMS. The frequency was varied from 1Hz to 10^6 Hz.

Electrochemical Characterization of the Nanosheets and Hydrogel. The CV and EIS (Electrochemical impedance spectroscopy) measurements were carried out on an electrochemical workstation (Gamry Reference 600, USA) at 100 mV/s. The MxNSPP nanosheets coated on a gold electrode were used as the working electrode; Pt and Ag/AgCl (KCl sat.) were used as the counter and reference electrodes, respectively. A PBS solution (0.1 M, pH = 7.4) was used as the electrolyte. The group with high polymeric degree PEDOT was electropolymerized under 0.9 V for 70 s. The potential was varied from −0.5 V to 0.60 V. EIS was measured as follows: The MxNSPP nanosheets were dispersed in PBS solution (1 mg mL^{-1}). A gold electrode was used as the working electrode; Pt and Ag/AgCl (KCl sat.) were used as the counter and reference electrodes, respectively. The nanosheets were electropolymerized on the gold electrode under 0.9 V for 40 s. The impedance of the MxNSPP nanosheet-coated electrode was measured. The AC voltage was 10 mV RMS. The impedance of the hydrogels was measured using a two-electrode setup on an electrochemical system (GAMRY Reference 600, USA). The hydrogels (R = 7 mm, L = 20 mm) were measured between two parallel gold electrodes.

PC12 Cell Proliferation and Differentiation with ES. ES was carried out as previously described (45). A pair of parallel gold electrodes were used to perform the in vitro ES. The PC12 cells (6×10^4 cells $sample^{-1}$) were seeded on the MxNS- and MxNSPP-coated coverslips, which were sterilized with 75% ethanol and UV. After culturing with complete medium (80% Roswell Park Memorial Institute (RPMI) 1640 medium, 1% penicillin/streptomycin solution, 10% HS, and 9% fetal bovine serum (FBS)) for 1 d, different ES potentials (0, 30, 60, and 120 mV) were applied to each group for 1.5 h, respectively. After 2 d of further culturing, the groups were fixed and stained with phalloidin (green) and DAPI (blue). The groups were observed with a slide scanner (VS120-S-W, OLYMPUS, Japan). The proliferation activities of the cells in the groups were evaluated using the MTT assay and measured with a microplate reader (H1M, BioTek, USA).

SC Proliferation and Migration. Coverslips were coated with the MxNS or MxNSPP nanosheets in a 0.4-mm grid pattern and sterilized with 75% ethanol and UV. S16 cells (6×10^4 cells $sample^{-1}$) were cultured on the coverslips in a 24-well plate with 400 μL of complete medium (90% Dulbecco's modified eagle medium (DMEM), 1% penicillin/streptomycin solution, and 9% FBS). After culturing for 48 h, the groups were fixed and stained with phalloidin (green) and DAPI (blue). SC migration was observed with a slide scanner (VS120-S-W, OLYMPUS, Japan). The viability and cytotoxicity of the groups were evaluated using the Calcein/PI assay and measured with a microplate reader (H1M, BioTek, USA).

Effects of MXene Coculture on PC12 Differentiation. Transwells were coated with different MXene nanosheets and sterilized with 75% ethanol and UV. S16 cells (6×10^3 cells $sample^{-1}$) were plated in the upper chambers of 24-well transwell plates (Corning, NY, USA; pore diameter = 8 μm), and PC12 cells (1.5×10^4 cells $sample^{-1}$) seeded on MXene coated coverslips were placed in the lower chambers. S16 cells (6×10^3 cells $sample^{-1}$) were plated in the upper chambers of 24-well transwell plates (Corning, NY, USA; pore diameter = 8 μm). After being seeded for 6 h, PC12 cells were cocultured for 2 d. PC12 cells were fixed and stained with phalloidin (green) and DAPI (blue). PC12 cell differentiation was observed with a slide scanner (VS120-S-W, OLYMPUS, Japan).

ROS-Scavenging Performance. Raw264.7 cells (6×10^4 cells $sample^{-1}$) were cultured on a 24-well plate with 500 μL of complete medium (90% RPMI 1640 medium, 1% penicillin/streptomycin solution, and 9% FBS). After culturing for 24 h, the groups were washed three times with serum-free medium. DCFH-DA was diluted with a serum-free medium at 1:1,000 to make the final concentration 10 μM, and 400 μL of DCFH-DA diluent was added into each group and loaded into cells at 37 °C for 30 min. Afterward, H_2O_2 (300 mM, 0.4 μL), together with MxNS, MxNSP, or MxNSP, was added to each group. After 20 min, each group was washed three times with serum-free medium. The groups were observed with a slide scanner (VS120-S-W, OLYMPUS, Japan).

Effects of Polarized Macrophages on SC Migration. Coverslips were coated with different MXene nanosheets and sterilized with 75% ethanol and UV. S16 cells (8×10^3 cells $sample^{-1}$) were plated in the upper chambers of 24-well transwell plates (Corning, NY, USA; pore diameter = 8 μm), and Raw264.7 cells (6×10^4 cells $sample^{-1}$) seeded on MXenes coated coverslips were placed in the lower chambers and precultured for 24 h. Transwell plates with S16 cells were then moved to Raw264.7 cells. After incubation for 6 h, the chambers were rinsed with PBS and fixed with 4% paraformaldehyde (PFA). Cells on the upper surface of the filter membranes were gently wiped off using cotton swabs, and the cells that had migrated to the lower surface of the membranes were stained with 0.5% crystal violet for 5 min and then imaged and counted.

Cell-Shape Analysis. Fluorescence images of phalloidin staining were used for analyzing cell shape. The long and short axes were manually measured for each cell using ImageJ software, as previously described (46). The long axis was calculated as the longest length of the cell. In contrast, the short axis was measured as the length of the axis perpendicular to the long axis and across the nucleus, and the elongation index was then calculated as the ratio of the long axis to the short axis and used for assessing the morphological changes of macrophages.

Real-Time PCR. RT-PCR of macrophages was carried out as previously described. Total RNA was extracted using a Trizol reagent (Beyotime) according to the manufacturer's instructions. The amount of RNA was measured using a NanoDrop ND-2000 UV-Visible spectrophotometer (Fisher Scientific). Then, 2 mg of total RNA was reverse transcribed into cDNA using the M-MLV reverse transcriptase (Beyotime) and oligo (BGI) primers. The PCR reactions were performed using the following oligonucleotide primers: VEGF-F, 5-CACACAGGATGGCTTGAAGA-3; and VEGF-R, 5-AGGGCAGAATCATCACGAAG-3. NGF-F, 5-CCCGAATCCTGTAGAGAGTGG-3; and NGF-R, 5-GACAAAGGTGTGAGTCGTGG-3. Arg1-F, 5-CAGAAGAATGGAAGAGTCAG-3; and Arg1-R, 5-CAGATATGCAGGGAGTCACC-3. IL-10-F, 5-ATTTGAATTCCCTGGGTGAGAAG-3; and IL-10-R, 5-CACAGGGGAGAAATCGATGACA-3. The relative expression of housekeeping gene in LPS-treated macrophages was determined by the delta Ct method.

ROS Induces MxNSPP Nanosheet further Oxidizing and Stacking In Vitro. Raw264.7 cells (6×10^4 cells $sample^{-1}$) were cultured on a 24-well plate with 500 μL of complete medium (90% RPMI 1640 medium, 1% penicillin/streptomycin solution, and 9% FBS). After culturing for 24 h, the Raw264.7 cells were washed three times with serum-free medium and incubated in serum-free medium with H_2O_2 (300 mM, 0.4 μL) for 30 min into ROS+ Raw264.7 cells. Then, ROS+ Raw264.7 cells were seeded on MxNSPP coated coverslip and cultured for 12 h. After washing off the cells on the coverslips, the MxNSPP-coated coverslips were measured with a micro-Raman Spectrometer (LabRam HR Visible, Horiba Jobin Yvon, France) on a 633-nm laser at 1 mW.

Antioxidation and Biodegradation Properties of the Nanosheets. The total antioxidant capacity of the nanosheets was measured with a Total Antioxidant Capacity Assay Kit (Beyotime). Peroxidase working solution (20 μL) was added to

each detection hole of 96-well plates. Deionized water (10 μL) or the nanosheet dispersion was added into the blank control hole; Trolox standard solution (10 μL) of various concentrations was into the standard curve detection hole. ABTS working solution (170 μL) was added into each hole and mixed gently. After 6 min of reacting in the dark, the absorption of the samples was measured using a microplate reader (H1M, BioTek, USA). The structure failure caused by ferric iron was measured by adding 2 mL of 0.5 g mL^{-1} FeCl3 dropwise into 10 mL of 3 mg mL^{-1} MxNSPP aqueous solution. The freeze-dried nanosheets were dispersed in 20 mL of deionized water (3 mg mL^{-1}). The dispersion was vacuum filtered into a membrane into a self-supporting membrane by vacuum suction filtration. Then, 64 mm^2 nanosheet self-supporting films were placed in a 9 mm cell culture dish. Two mL of 1% hydrogen peroxide was added dropwise to the nanosheets till fully immersed. The freeze-dried MxNSPP nanosheets were dispersed in 20 mL of deionized water (3 mg mL^{-1}). The dispersion was vacuum filtered into a self-supporting membrane. Then, 100 mm^2 MxNSPP membrane was placed in 50 mL PBS, in Nitrogen or air, and heated at 85 °C. The degradation process was observed and recorded.

Induction of SNC. SNC models were conducted in 6- to 8-wk-old C57BL/6J mice as previously described. Mice were anesthetized with isoflurane (5% induction, 2% maintenance) and shaved on the hind limbs. An ophthalmic solution was applied to the eyes to prevent drying. An incision was made at the right thigh. The BF and gluteus superficialis were separated by blunt dissection to expose the sciatic nerve. The SNC was performed orthogonally two times at 2N for 10 s (15s for the reinnervation experiment) using 5-mm surgery forceps, and the wound was closed by sutures. The contralateral side was left untouched. For all experiments, the part distal to the nerve injury was used for analysis.

Jet-Injection and ES of MxNSPP Interface. The MxNSPP nanosheets were dispersed in sterilized saline at 5 mg mL^{-1}. Mice were anesthetized with isoflurane (5% induction and 2% maintenance), shaved on the hind limbs, and put on a heating pad to maintain body temperature. An ophthalmic solution was applied to the eyes to prevent drying. The outer thigh of the mice was shaved and disinfected. The mouse's leg was moved to observe the white sciatic nerve fiber under the skin. For ES at SN, the nanosheet dispersion was injected to the proximal part of the nerve injury with the jet injector. The total injection volume is about 30 μL. Twelve hours later, a polyurethane film was used to isolate the right thigh skin, leaving a whole opening (R = 0.5 mm) on the injection sight. An adhesive PE (R = 2 mm) was placed at the injection site as a cathode, and an adhesive PE (R = 2 mm) was placed at the homolateral ankle as an anode. ES was performed with a direct current pulse stimulation for 30 min, with an electrical voltage range of 3 V and a frequency of 20 Hz. The ES was conducted every other day on the injected groups. For ES at hindlimb ST36 (Zusanli) acupoints, the experiments were based on the previously described. The nanosheet dispersion was injected to the regions located about 4 mm down from the knee joint and about 2 mm lateral to the anterior tubercle of the tibia with the jet injector. Twelve hours later, a polyurethane film was used to isolate the right thigh skin, leaving a whole opening (R = 0.5 mm) on the injection sight. An adhesive PE (R = 2 mm) was placed at the injection site; an adhesive PE (R = 2 mm) was placed on the skin above the distal gluteal muscles without isolation. Note that the electroacupuncture group with the conducting patches on the skin above distal gluteal muscles and a needle at ST36 was different from the focal electric stimulation mode, with the positive and negative electric needles separated by 1 mm used by Shenbin Liu et al. For studying ES effects on LPS-induced systemic inflammation and mortality, ES was performed 15 min before LPS injection. For studying ES-evoked c-Fos induction in DMV and rVLM, ES was performed for 15 min, and 2 h later, the mice were perfused for tissue collection.

In Vivo Acute Toxicity, Metabolism, and Biodistribution Assessment. Mice were divided into three groups (n = 5), anesthetized with isoflurane (5% induction and 2% maintenance), shaved on the hind limbs, and put on a heating pad to maintain body temperature. The outer thigh of the mice was shaved and disinfected. The nanosheet dispersion at a concentration of 5 mg mL^{-1} was injected into the distal part of the nerve injury proximal with the jet injector. The mice were randomly picked out and continually killed. The major organs (heart, liver, spleen, lung, and kidney) were harvested for section and stained by HE 7 d after injection. The mice were executed and dissected after injecting the nanosheets into the sciatic nerve at 4 and 24 h (n = 3). The major organs (liver and spleen) were weighted and dissociated by aqua regia. The ICP-OES test quantitatively analyzed Ti content in major organs and tumor tissue.

Track-Walking Movement Analysis. The mice were allowed to walk down a wooden alley (5.0 × 8.0 × 45 cm^3). The floor of the alley was covered with white paper. Acrylic paint was applied to the mice's plantar surface to visualize the footprints. This process was repeated three times until clear footmarks were obtained. From the footprints, the following parameters were obtained: distance from the heel to the top of the third toe (print length, PL), the distance between the first and the fifth toe (toe spread, TS), and distance from the second to the fourth toe (intermediary toe spread, IT). These measures were made for both the non-operated foot, including non-operated print length (NPL), non-operated toe spread (NTS), non-operated intermediary toe spread (NIT), experimental print length (EPL), experimental toe spread (ETS), and experimental intermediary toe spread (EIT). The sciatic function index (SFI) was calculated fromprint length factor (PLF), toe spread factor (TSF), and intermediary toe-spread factor (ITF) with thefollowing method:

$$SFI = (-38.3 \times PLF) + (109.5 \times TSF) + (13.3 \times ITF) - 8.8$$

$$PLF = (EPL - NPL)/NPL$$

$$TSF = (ETS - NTS)/NTS$$

$$ITF = (EIT - NIT)/NIT$$

Motor and Sensory Nerve Conduction Velocities Measurement. As previously described, we used the Hoffman (H-reflex) to determine motor and sensory conduction velocities. The mice were anesthetized with isoflurane. A pair of needle electrodes were implanted through the surface skin of the proximal metatarsal bone as a recording electrode and placed on the foot pad at the root of the thumb of the hind limb as a reference electrode. A ground electrode was placed in the tail. A pair of needle electrodes were implanted to stimulate either the sciatic nerve at the hip or the tibial nerve at the ankle. Square-wave pulses (0.1 to 0.3 ms) were used to stimulate the nerves. Stimulus amplitude was slowly increased until either the H-reflex or M-wave was first discernible. The short-latency M-wave represents electrical muscle activity evoked by direct stimulation of the motor nerves to the plantar muscles. The latencies between the stimulus artifact and the initiation of the M-wave and H-reflex in the muscle were determined for both stimulus locations. The nerve conduction distance was determined by measuring the distance between the most distal stimulating electrode at the ankle and that at the hip after straightening the leg. The motor and sensory conduction velocities were calculated from the following:

Motor conduction velocity = Distance between stimulating electrodes/Latency of M-wave (hip) – Latency of M-wave (ankle)

Sensory conduction velocity = Distance between stimulating electrodes/Latency of H-wave (ankle) – Latency of H-wave (hip)

Histology. Animals were killed with CO_2 and then transcardially perfused with 4% PFA. The hindlimbs with the injected interface and brains were dissected and then post-fixed in 4% PFA for 48 h. Fixed hindlimbs were rinsed with PBS and decalcified in 10% Ethylenediaminetetraacetic acid (EDTA) at 4 °C for 2 wk. Tissues were cryopreserved in 30% sucrose in PBS overnight and then embedded in Tissue-Tek OCT compound (Sakura Finetek). Immunohistochemistry on 30-μm-thick sections through collected tissues was performed as previously described with the following antibodies: goat anti-ChAT (1:500, AB144P), c-Fos (1:500, 2250S), S100 (1:500, ab52642), PGP9.5 (1:500, ab108986), Beta III tubulin (1:500, ab76286), CD206 (1:500, 24595T), CCR7 (1:500, MAB3477-SP), donkey anti-goat 594 (1:500, ab150132), donkey anti-rabbit 488 (1:500, A32790), goat anti-rabbit 488 (1:500, A-11008), and goat anti-rabbit 568 (1:500, ab175471). The sections were acquired using a slide scanner (VS120-S-W, Olympus, Japan) or a confocal laser scanning microscope (LSM 900, Zeiss, Germany). The MxNSPP deposition images were converted from bright-field images and merged into fluorescent images using Photoshop.

Sample Clearing. The mice were executed 5 d after jet injection and then transcranial perfused with 4% PFA. The ST36 tissues were fixed in 4% PFA solution for 48 h, washed with PBS, and decalcified in 10% EDTA for 2 wk. The tissues underwent gradient dehydration in ethanol for 2 d, degreased in acetone for 1.5 d, and gradient rehydrated in PBS solution. A solution with high RI was prepared by mixing 50 wt% iohexol (Hisyn Pharmaceutical), 23 wt% urea (Sangon), 11 wt% 2,2′,2″,-nitrilotriethanol (Sigma), and 16 wt% distilled water; the final RI of the PuClear RI-matching solution was 1.52. Before imaging, samples were incubated in this solution for at least 5 h to facilitate optical transparency.

In Vivo Serum Cytokine and Catecholamine Analyses. Mice were intraperitoneally injected with an LD80 (80% lethality rate) dose of LPS (8 mg kg^{-1} for C57BL/6J male mice) after ES at ST36. Blood from the eyeball was collected 1.5 h after LPS injection at the indicated time points, allowed to clot for 1.5 h at room temperature, and then centrifuged at 2,500 g for 15 min at 4 °C. The supernatant serum was collected and assessed by using the ELISA kit (Jiangsu Meimian Industrial Co., Ltd), following the manufacturer's instructions. For serum catecholamine measurements, blood was collected 15 min after ES at ST36, allowed to clot for 1.5 h at room temperature, and centrifuged at 2,500 g for 15 min at 4 °C. The supernatant serum was collected, transferred to regular tubes, and analyzed using the ELISA kit (BYabscience), following the manufacturer's instructions.

Heat and Mechanical Pain Threshold Test. Before SNI or injection, two baselines were measured with graded von Frey nylon filaments. Mice were kept in clear PMMA boxes with a 0.7 cm mesh flooring to habituate for 15 min before testing. For the SNC study, Von Frey filaments were applied in ascending order to the surface of the hind paws. The withdrawal threshold was defined as the lowest force leading to at least three withdrawals in five trials. For the injection pain study, the experiments were carried out as previously described. For hot plate tests, hind paw lifting and flinching were used to determine withdrawal latencies. For each hot plate test, a cutoff condition was established with a temperature of 50 °C and a maximum duration of one minute.

Physiological Recording and Behavioral Test. For neural signal recording in a moving animal, the jet-injected MxNSPP neural interface was implanted in the SN as mentioned above. Another conducting patch was placed on the lateral side of the hind limb at the knee. The neural signal and the two-dimensional motion data were recorded synchronously. The motion system was composed of a high-speed digital camera and a treadmill running in 10 m min^{-1}. The digital camera was positioned perpendicular to the walking trace, and the images were recorded at 240 frames s^{-1}. The anatomical landmarks were denned to the two conducting patches, ankle, and fifth metatarsal joint.

Data, Materials, and Software Availability. Original data including material characterization, cell culture, imaging, in vivo electrophysiology data have been deposited in Figshare: Carrier-Free Jet-Injected Neural Interface for Non-InvasiveLocal and Systemic Immunomodulation Supporting Data (47).

ACKNOWLEDGMENTS. We thank Hao Huang and Zhengsheng Li for their help with XRD and Raman spectroscopy measurement. This research was supported by Key-Area Research and Development Program of Guangdong Province (2018B030331001, 2018B030338001), Natural Science Foundation of China Grant (31930047, 31700936), National Key R&D Program of China (2017YFC1310503, 2020YFC2008503), Scientific and Technological Innovation 2030 Key Project (2022ZD0209800), the Strategic Priority Research Program of Chinese Academy of Science (XDB32030103), National Special Support Grant (W02020453), NSFC-Guangdong Joint Fund (U20A6005), the Guangdong Provincial Grant (2017A030310496), Shenzhen Infrastructure for Brain Analysis and Modeling (ZDKJ20190204002), Shenzhen Governmental Basic Research Grants (JCYJ20160531174444711).

Author affiliations: [a]Brain Cognition and Brain Disease Institute, Shenzhen Institute of Advanced Technology, Chinese Academy of Sciences, Shenzhen 518055, China; [b]Chinese Academy of Sciences Key Laboratory of Brain Connectome and Manipulation, Shenzhen Institute of Advanced Technology, Chinese Academy of Sciences, Shenzhen 518055, China; [c]Guangdong Provincial Key Laboratory of Brain Connectome and Behavior, Shenzhen Institute of Advanced Technology, Chinese Academy of Sciences, Shenzhen 518055, China; [d]Shenzhen-Hong Kong Institute of Brain Science, Shenzhen Fundamental Research Institutions, Shenzhen 518055, China; [e]Faculty of Life and Health Sciences, Shenzhen Institute of Advanced Technology, Chinese Academy of Sciences, Shenzhen 518055, China; [f]University of Chinese Academy of Sciences, Beijing 100049, China; [g]Department of Biomedical Engineering, Columbia University, New York, NY 10027; [h]Department of Electrical Engineering, Columbia University, New York, NY 10027; [i]Nano Science and Technology Institute, University of Science and Technology of China, Suzhou 215123, China; and [j]Center for Integrative Imaging, Hefei National Laboratory for Physical Sciences at the Microscale, and School of Life Sciences, University of Science and Technology of China, Hefei 230026, China

Author contributions: B.S. and Z.D. designed research; B.S., S.Z., and M.G. performed research; B.S. and Z.D. analyzed data; D.K. partially supervised the revision-stage experiments, refined the revision manuscript; L.W., G.-Q.B., and Z.D. supervised research; and B.S., D.K., L.W., G.-Q.B., and Z.D. wrote the paper.

1. E. E. Meyers, A. Kronemberger, V. Lira, K. Rahmouni, H. M. Stauss, Contrasting effects of afferent and efferent vagal nerve stimulation on insulin secretion and blood glucose regulation. *Physiol. Rep.* **4**, e12718 (2016).
2. B. Bonaz *et al.*, Chronic vagus nerve stimulation in Crohn's disease: A 6-month follow-up pilot study. *Neurogastroenterol. Motil* **28**, 948–953 (2016).
3. F. A. Koopman *et al.*, Vagus nerve stimulation inhibits cytokine production and attenuates disease severity in rheumatoid arthritis. *Proc. Natl. Acad. Sci. U.S.A.* **113**, 8284–8289 (2016).
4. S. N. Liu *et al.*, A neuroanatomical basis for electroacupuncture to drive the vagal-adrenal axis. *Nature* **598**, 641–645 (2022).
5. A. Balakrishnan *et al.*, Insights into the role and potential of schwann cells for peripheral nerve repair from studies of development and injury. *Front. Mol. Neurosci.* **13**, 608442 (2021).
6. S. L. Wang *et al.*, Intrinsically stretchable electronics with ultrahigh deformability to monitor dynamically moving organs. *Sci. Adv.* **8**, eabl5511 (2022).
7. Y. W. Jiang *et al.*, Topological supramolecular network enabled high-conductivity, stretchable organic bioelectronics. *Science* **375**, 1411–1417 (2022).
8. K. I. Song *et al.*, Adaptive self-healing electronic epineurium for chronic bidirectional neural interfaces. *Nat. Commun.* **11**, 4195 (2020).
9. H. Seo *et al.*, Durable and fatigue-resistant soft peripheral neuroprosthetics for in vivo bidirectional signaling. *Adv. Mater.* **33**, e2007346 (2021).
10. F. Darlot, A. Artuso, N. Lautredou-Audouy, D. Casellas, Topology of Schwann cells and sympathetic innervation along preglomerular vessels: A confocal microscopic study in protein S100B/EGFP transgenic mice. *Am. J. Physiol. Renal Physiol.* **295**, F1142–F1148 (2008).
11. L. Chen, X. Y. Dai, W. Feng, Y. Chen, Biomedical applications of MXenes: From nanomedicine to biomaterials. *Acc. Mater. Res.* **3**, 785–798 (2022).
12. S. Iravani, R. S. Varma, MXene-Based composites as nanozymes in biomedicine: A perspective. *Nano-Micro Lett.* **14**, 213 (2022).
13. D. Wu *et al.*, Molecular insights into MXene destructing the cell membrane as a "nano thermal blade". *Phys. Chem. Chem. Phys.* **23**, 3341–3350 (2021).
14. Y. Li *et al.*, Graphene microsheets enter cells through spontaneous membrane penetration at edge asperities and corner sites. *Proc. Natl. Acad. Sci. U.S.A.* **110**, 12295–12300 (2013).
15. S. Doo *et al.*, Mechanism and kinetics of oxidation reaction of aqueous Ti(3)C(2)T(x) suspensions at different phs and temperatures. *ACS Appl. Mater. Interfaces* **13**, 22855–22865 (2021).
16. H. Wang *et al.*, Surface modified MXene Ti3C2 multilayers by aryl diazonium salts leading to large-scale delamination. *Appl. Surface Sci.* **384**, 287–293 (2016).
17. H. Wang *et al.*, In situ polymerized Ti3C2Tx/PDA electrode with superior areal capacitance for supercapacitors. *J. Alloys Compd.* **778**, 858–865 (2019).
18. A. Sarycheva, Y. Gogotsi, Raman spectroscopy analysis of the structure and surface chemistry of Ti3C2Tx MXene. *Chem. Mater.* **32**, 3480–3488 (2020).
19. T. Hu *et al.*, Vibrational properties of Ti3C2 and Ti3C2T2 (T = O, F, OH) monosheets by first-principles calculations: A comparative study. *Phys. Chem. Chem. Phys.* **17**, 9997–10003 (2015).
20. S. Rafiq *et al.*, Novel room-temperature ferromagnetism in Gd-doped 2-dimensional Ti3C2Tx MXene semiconductor for spintronics. *J. Magn. Magn. Mater.* **497**, 165954 (2020).
21. X. Li *et al.*, Ti3C2 MXenes modified with in situ grown carbon nanotubes for enhanced electromagnetic wave absorption properties. *J. Mater. Chem. C* **5**, 4068–4074 (2017).
22. C. Chen *et al.*, Charge transfer induced polymerization of EDOT confined between 2D titanium carbide layers. *J. Mater. Chem. A* **5**, 5260–5265 (2017).
23. J. Liu *et al.*, Genetically targeted chemical assembly of functional materials in living cells, tissues, and animals. *Science* **367**, 1372–1376 (2020).
24. S. Nie, Z. Li, Y. Yao, Y. Jin, Progress in synthesis of conductive polymer poly(3,4-Ethylenedioxythiophene). *Front. Chem.* **9**, 803509 (2021).
25. M. N. Gueye, A. Carella, J. Faure-Vincent, R. Demadrille, J.-P. Simonato, Progress in understanding structure and transport properties of PEDOT-based materials: A critical review. *Prog. Mater. Sci.* **108**, 100616 (2020).
26. D. Gan *et al.*, Graphene oxide-templated conductive and redox-active nanosheets incorporated hydrogels for adhesive bioelectronics. *Adv. Funct. Mater.* **30**, 1907678 (2020).
27. M. Greaves, M. Mende, J. Wang, W. Yang, S. Barg, Investigating the rheology of 2D titanium carbide (MXene) dispersions for colloidal processing: Progress and challenges. *J. Mater. Res.* **36**, 4578–4600 (2021).
28. H. Miyazaki, S. Atobe, T. Suzuki, H. Iga, K. Terai, Development of pyro-drive jet injector with controllable jet pressure. *J. Pharm Sci.* **108**, 2415–2420 (2019).
29. B. D. Hemond, A. Taberner, C. Hogan, B. Crane, I. W. Hunter, Development and performance of a controllable autoloading needle-free jet injector. *J. Med. Devices* **5**, 015001 (2011).
30. L. M. Ferrari, U. Ismailov, F. Greco, E. Ismailova, Capacitive coupling of conducting polymer tattoo electrodes with the skin. *Adv. Mater. Interfaces* **8**, 2100352 (2021).
31. X. Strakosas *et al.*, Metabolite-induced in vivo fabrication of substrate-free organic bioelectronics. *Science* **379**, 795–802 (2023).
32. S. Metwally, U. Stachewicz, Surface potential and charges impact on cell responses on biomaterials interfaces for medical applications. *Mater. Sci. Eng. C Mater. Biol. Appl.* **104**, 109883 (2019).
33. M. Tallawi *et al.*, Strategies for the chemical and biological functionalization of scaffolds for cardiac tissue engineering: A review. *J. R. Soc. Interface* **12**, 20150254 (2015).
34. S. Cai *et al.*, Recent advance in surface modification for regulating cell adhesion and behaviors. *Nanotechnol. Rev.* **9**, 971–989 (2020).
35. J. Y. Cai *et al.*, GelMA-MXene hydrogel nerve conduits with microgrooves for spinal cord injury repair. *J. Nanobiotechnol.* **20**, 460 (2022).
36. O. S. Manoukian *et al.*, Functional polymeric nerve guidance conduits and drug delivery strategies for peripheral nerve repair and regeneration. *J. Control Release* **317**, 78–95 (2020).
37. K. R. Jessen, R. Mirsky, The repair Schwann cell and its function in regenerating nerves. *J. Physiol.* **594**, 3521–3531 (2016).
38. K. V. Panzer *et al.*, Tissue engineered bands of BÃ¼ngner for accelerated motor and sensory axonal outgrowth. *Front. Bioeng. Biotechnol.* **8**, 580654 (2020).
39. C. R. Carvalho, J. Silva-Correia, J. M. Oliveira, R. L. Reis, Nanotechnology in peripheral nerve repair and reconstruction. *Adv. Drug Deliv. Rev.* **148**, 308–343 (2019).

40. R. Li *et al.*, Growth factors-based therapeutic strategies and their underlying signaling mechanisms for peripheral nerve regeneration. *Acta Pharmacol. Sin* **41**, 1289–1300 (2020).
41. X. S. Zheng *et al.*, A superoxide scavenging coating for improving tissue response to neural implants. *Acta Biomater.* **99**, 72–83 (2019).
42. M. Mittal, M. R. Siddiqui, K. Tran, S. P. Reddy, A. B. Malik, Reactive oxygen species in inflammation and tissue injury. *Antioxid. Redox Signal* **20**, 1126–1167 (2014).
43. S. Javeed, A. H. Faraji, C. Dy, W. Z. Ray, M. R. MacEwan, Application of electrical stimulation for peripheral nerve regeneration: Stimulation parameters and future horizons. *Interdiscip. Neurosurg.* **24**, 101117 (2021).
44. S. Liu *et al.*, A neuroanatomical basis for electroacupunctureÂ to drive the vagal-adrenal axis. *Nature* **598**, 641–645 (2021).
45. C. Zhang *et al.*, Graphene trapped silk scaffolds integrate high conductivity and stability. *Carbon* **148**, 16–27 (2019).
46. Z. J. Du *et al.*, Ultrasoft microwire neural electrodes improve chronic tissue integration. *Acta Biomater.* **53**, 46–58 (2017).
47. B. Sha *et al.*, Doping-induced assembly interface for non-invasive in vivo local and systemic immunomodulation. Figshare. https://figshare.com/s/1048bf62c920630cd985. Deposited 20 April 2023.